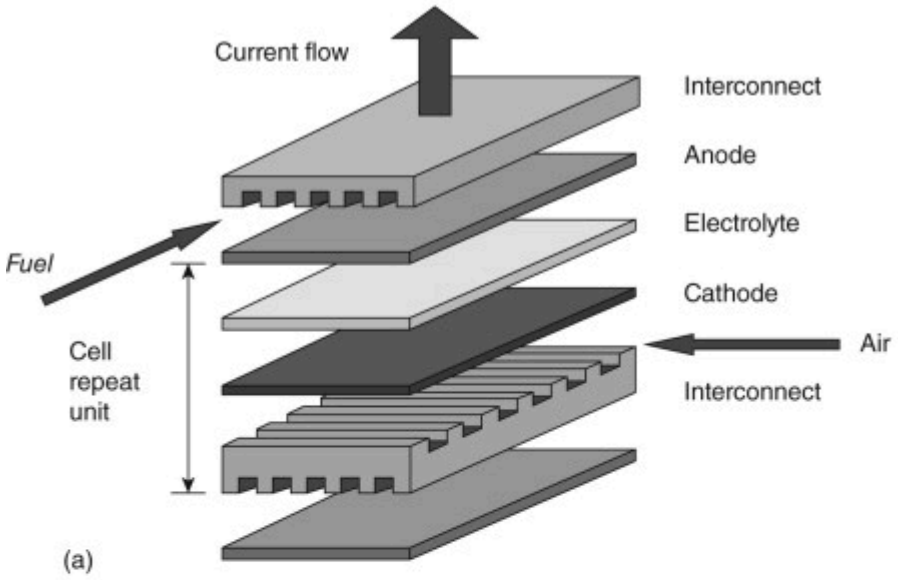

[1]

Performance Evaluation of Candidate Materials For Solid Oxide Cell Interconnects

- Corrosion of interconnects at 800 °C in 3%H_2O Air Atmospheres

Bachelor's thesis in chemical engineering

Igor Mitrović

Department of Chemistry and Chemical Engineering

CHALMERS UNIVERSITY OF TECHNOLOGY

Gothenburg 2024

Thesis for bachelor's degree

Performance Evaluation of Candidate Materials For Solid Oxide Cell Interconnects

Igor Mitrović

CHALMERS
UNIVERSITY OF TECHNOLOGY

Department of Chemistry and Chemical Engineering

CHALMERS UNIVERSITY OF TECHNOLOGY

Performance Evaluation of Candidate Materials For Solid Oxide Cell Interconnects -
-Corrosion of interconnects at 800 °C in 3%H_2O Air Atmospheres (chromium evaporation)

Igor Mitrović

Supervisor: Thorbjørn Krogsgaard, Chemistry

Examiner: Jesper Liske, Chemistry

Bachelor's Thesis 2024

Department of Chemistry and Chemical Engineering

Chalmers University of Technology

SE-412 58 Gothenburg Telephone +46 31 772 1000

Cover: Schematic representation of a Solid Oxide Fuel Cell

Gothenburg 2024

Acknowledgements

I would like to take this opportunity to acknowledge the people who have made this thesis possible and have contributed to my growth both academically and personally during my thesis here at Chalmers University of Technology.

First I would like to thank my examiner Associate Professor Jesper Liske and my Supervisor Doctoral Student Thorbjørn Krogsgaard, for their guidance, support, and encouragement throughout my thesis project. Your expertise, insights, and constructive feedback have been instrumental in shaping the direction and quality of my work. I am grateful for the opportunity to complete my bachelor studies with such an interesting thesis.

I would also like to extend my sincere thanks to my officemates, Joachim Rödbro and Petter Jacobsson. The numerous discussions, exchanging of ideas, and the collaborative atmosphere enriched my experience. The camaraderie, fun, and laughter we shared have made this journey not only productive but also immensely enjoyable. Your support and friendship have been invaluable, and I cherish the creative work environment we built together. I would also like to extend a special thanks to my Mentor Derk De Munich for giving me advice on structure and ideas for presenting the project.

A special thank you goes to Malin Fuhrman for showing preparation of samples, denuder tubes and analysis of chromium evaporation samples. I would also like to extend my sincere thanks to the administrative staff, whose assistance has given me the opportunity to access all the necessary facilities.

I am also deeply grateful to my family – my mom, dad, sister, and grandparents – for their unwavering love, support, and encouragement throughout my degree project and studies. Your belief in me has been a constant source of strength and motivation. I cannot thank you enough for your faith in my abilities.

Thank you all once again. This would not have been possible without your collective support and encouragement.

Abstract

This thesis examines the oxidation kinetics and the chromium evaporation of possible SOFC interconnect materials at 800 °C in air with 3% water vapor. The selected materials are AISI 441, AISI 446, Nirosta (Industrial Melt 1), and Crofer 22 APU. The study shows that the oxidation kinetics of these steels are varied, with AISI 441 and Crofer 22 APU showing dissimilar behaviors compared to AISI 446 and Nirosta (IM 1). Among the materials, Crofer 22 APU exhibits a mass loss, indicating unique oxidation kinetics. Chromium evaporation rates also differ, with AISI 441 showing the highest average evaporation rate and Crofer 22 APU the lowest, suggesting better protective properties of the oxide scale formed on the surface of Crofer 22 APU. The findings highlight that Crofer 22 APU, due to its protective oxide scale, is the most promising candidate for SOFC interconnects under the tested conditions. Furthermore, the possibility of using Nirosta (IM 1) or AISI 446 materials as cheaper counterparts although, they exhibit somewhat higher values of the chromium emission rate over time in comparison with Crofer 22 APU.

Acronyms

AFC	-	Alkaline Fuel Cell
BOP	-	Balance Of Plantes
FC	-	Fuel Cell
MCFC	-	Molten carbonate fuel cell
PEMFC	-	Proton exchange membrane fuel cell
SEM	-	Scanning Electron Microscopy
S/PAFC	-	Sulfuric and Phosphoric Acid Fuel Cell
SOC	-	Solid Oxide Cell
SOFC	-	Solid Oxide Fuel Cell
TPB	-	Three Phase Boundary
WA	-	AISI 441
WC	-	Crofer 22 APU
WD	-	Nirosta (Industry Melt 1)
WE	-	AISI 446

Contents

1 Introduction

1.1 Background

Increasing energy demands and a growing world population drives research forward in a multitude of sectors. From sustainable farming to more sustainable energy solutions, higher living standards are made every year. A critical challenge is access to clean, efficient and reliable energy [2]. As the energy demand increases, solutions and designs that don't compromise the environment must be further studied. Among solar, wind and hydroelectric power, fuel cells emerge as a promising technology. Converting chemical energy into electricity with higher conversion rates and fewer environmental effects than other options [2]. The commercialization potential of solid oxide cells (SOCs) is significant, but their lifetime and cost are currently holding the technology back. A vital part of a SOC is the interconnect which is what electrically connects individual cells of a fuel cell stack. Interconnects and their degradation are one of the main contributors to the cost of a SOC. Historically ceramic materials have been used for the interconnects, but today ferritic stainless steels (FSS) are used. FSS interconnects are more cost-effective than the ceramics, but degrade under the harsh operation temperatures in an SOC. As the FSS degrades certain corrosion phenomena have been observed, like chromium evaporation and continuous oxide scale growth. These phenomena negatively affect the performance of a SOC as the chromium vapor poisons the cathode and the oxide scale increases the electrical resistance of the FSS. To unlock the potential of SOCs it is important to investigate different FSS and improve the understanding of the mechanisms behind chromium evaporation and continuous oxide scale growth. All to better understand how to reduce their significance.

1.2 Aim & Goal

The goal of this thesis project is to evaluate the performance of the different ferritic stainless steel (FSS) materials, AISI 441, AISI 446, Nirosta (Industrial melt 1) and Crofer 22 APU, as potential interconnects for solid oxide cells (SOCs). The focus will be on their behavior at a high temperature of 800 degrees celsius in an air atmosphere containing 3% water vapor. The

primary objectives include comparing and analyzing oxidation kinetics and chromium evaporation rates of the materials. Additionally, the project aims to investigate the surface morphology of the FSS samples using a scanning electron microscope (SEM) to explore the grain boundaries on the surface.

1.3 Limitations

1. Time Constraints: Due to the duration of the bachelor thesis project being limited to one study period (100%), there are limitations on the amount of experimental work and analysis that can be conducted. Prioritizing key objectives and allocating resources effectively within the given timeframe is essential. Because of the limited time frame SEM may not be performed.

2. Long-Term Degradation Effects: The experimental work primarily focuses on short-term evaluations of oxidation kinetics and chromium evaporation rates. Long-term degradation effects, such as cyclic exposure to operating conditions or extended exposure durations, may have additional implications for material performance and reliability in practical SOC applications. These long-term effects may not be fully captured within the scope of the project.

3. Interconnect Integration: The project primarily focuses on evaluating the intrinsic properties of FSS materials in isolation. However, in real-world SOC applications, interconnects are integrated into a complex system with other components (e.g., electrolytes, electrodes). The performance of the interconnects may be influenced by interactions with these other components, which may not be fully captured in the experimental setup.

2 Theory

Fuel cells and electrolysers have a long standing history spanning around 200 years [3]. It was British scientists Sir Anthony Carlisle and William Nicholson who first described water electrolysis in 1800 [3]. The discovery came from at the time a new invention made by Alessandro Volta later named the voltaic pile [3]. In 1839, Sir William Grove and German scientist Christian Friedrich Schönbein independently discovered the phenomenon of reverse electrolysis [3]. To prove the electrochemical reaction between hydrogen and oxygen a gas battery was used to produce an electric current [3]. The fuel cell, a device used to convert chemical energy into electrical energy, had its first working prototype invented by William Robert Grove [3]. The device utilized platinum electrodes submerged in a dilute sulfuric acid solution and consisted of fifty electrode pairs, capable of generating voltage, producing sparkes and decomposing water to its constituents [3]. Grove's earlier speculation about series-connected cells to decompose water were now confirmed [3]. The findings mark a significant milestone in the development of fuel cell technology [3]. Further contributions were made towards the theoretical understanding of fuel cells in the 20th century by Willhem Ostwald [3].

2.1 Fuel cells

Fuel cells are used to produce electrical energy by harnessing electrochemical energy [3]. In essence fuel cell (FC) operation is similar to a battery with a slight difference that the fuel is stored outside of the cell [3]. This means that the performance of the fuel cell is limited by the availability of the fuel and oxidant [3]. As mentioned fuel cells are continuously operating batteries and generate their electricity from the given fuel source (ex. Hydrogen). Figure 1 shows a schematic representation of a fuel cell and its ion flow direction. From figure 1 the following basic equations (1-3) can be derived from a fuel cell operating with hydrogen as its fuel:

$$H_2(g) + \frac{1}{2}O_2(g) \rightarrow H_2O(g) + energy \quad (1)$$

$$Cathode: \frac{1}{2}O_2 + 2e^- \rightarrow O^{2-} \quad (2)$$

$$Anode: H_2 + O^{2-} \rightarrow H_2O + 2e^- \quad (3)$$

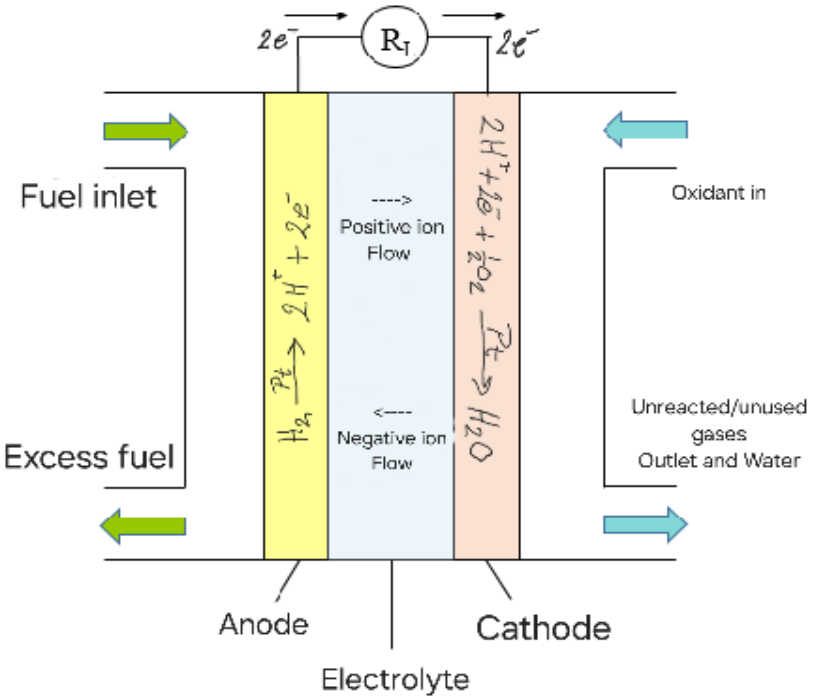

Figure 1: Schematic representation of a fuel cell/electrolyser and the reactions taking place, adapted from [2].

The half reactions for combustion of hydrogen is seen in equation 1. Reduction reaction is performed at the cathodic site and represented by equation 2 while oxidation is performed in the anodic end represented by equation 3.

The following materials are widely used in Fuel cells (FC), anode, cathode, electrolyte. The electrolyte separates the anode and cathode from one another and only facilitates diffusion of ions in one direction, all while limiting electron transfer and forcing electrons through an external circuit between the anode and cathode. The electron flow forced through the external circuit generates an electric current that is utilized to power other appliances.

In contrast to traditional combustion engines the FC directly converts chemical energy into electrical energy instead of creating heat and using that to create mechanical energy and ultimately electrical energy. Fuel cells also come in different variants with different operating temperatures and fuel tolerance.

Fuel cells are differentiated by their electrolyte or operating temperature.

1. Alkaline fuel cell (AFC)
2. Sulfuric and phosphoric acid fuel cell (S/PAFC)
3. Proton exchange membrane fuel cell (PEMFC)
4. Molten carbonate fuel cell (MCFC)
5. Solid oxide fuel cell (SOFC)

Despite the difference in temperature, fuel sources and electrolytes all fuel cells operate on the same electrochemical principles [4]. This study focuses on the Solid oxide fuel cell (SOFC) and will be described more in section 2.2.

2.2 Solid Oxide Fuel cells (SOFC)

The solid oxide fuel cell (SOFC) is a solid state device that operates with an ion-conducting electrolyte and two porous electrodes (anode and cathode) in order to generate electricity from a variety of fuel sources [2,3]. The SOFC only operates with two phases (gas and solid) avoiding the complications associated with liquid electrolytes; they do however present unique challenges due to the harsh operating conditions requiring high standards on the materials used [2]. In essence all fuel cells work on the same principles and only vary from each other with respect to temperature, fuel source and electrolyte. A solid oxide cell (SOC) uses ceramic material as an electrolyte and has a high operating temperature of 700-1000 °C. The high temperature allows for internal reforming, a process that converts hydrocarbon fuels into hydrogen-rich gas directly within the fuel cell stack itself, and promotes rapid kinetics without precious materials [3].

2.2.1 Anode & Cathode electrodes

As per figure 1 the basic requirement for the anodic region in a FC is to provide a sufficient amount of active sites for the fuel to be oxidized [5]. The simple reaction given in figure 1 shows three phases: gas (H_2), ion (H^+) and electrons (e^-) meaning that a three phase carrier must exist in order to facilitate transport of ions from the electrolyte and electrons to an external circuit [5]. The three phase carrier is often called the three phase boundary (TPB). For a solid oxide fuel cell (SOFC), the anode is made from a porous ion and electron

conductive material [5]. This dual conductivity allows for ions to diffuse into the electrolyte and for electrons to travel via an external circuit, the ion and electron conductive material can be a single phase or a composite phase boundary; this design is critical for the anode and requires complex micro structures [5]. Given the high operating temperatures of a solid oxide cell (SOC) the anode must not only have good ion and electron conductivity but also stability to ensure a long lifespan. The anodes also operate under fluctuating oxygen partial pressure (pO_2) [5]. Preparation of the anodes are done in air meaning a high pO_2, and then reduced at high temperature lowering the pO_2[5]. Therefore the anode must be able to withstand high temperatures and fluctuating pO_2.

The anode is however not the only vital part of the SOFC, another component carrying an important role is the cathode. The high temperature environment in SOFC promotes electrode reaction without the use of precious metal catalysts lite platinum [5]. This does however not mean that the cathodic site can be made out of any material, like with the anode it has certain requirements. The required properties are a high catalytic activity, chemical mechanical, morphological stability (also compatibility with components) and electron/ion conductivity [5].

2.2.2 Electrolyte

The electrolyte serves as the ion conducting (diffusion) material. Ion diffusion through the electrolyte is driven by the concentration gradient and electrochemical potential difference. This means that the anodic side has a net positive charge while the cathodic site has a net negative charge (at startup). In order for the reaction to take place on the cathodic site the electrolyte must have a high selectivity towards diffusion of positively charged ions. The diffusion can also be controlled by pore size. The electrolyte serves as a barrier for gas diffusion preventing hydrogen molecules from moving to the cathodic site before being oxidized [6]. Thanks to the electrolyte barrier, half cell reactions occur at the anode and cathode promoting ion diffusion through the electrolyte layer [6]. When electrolytes are chosen, their ion conductivity and impermeability of gasses and the electric conductivity is evaluated [6].

2.2.3 Interconnects

Inorder to achieve higher voltage (the driving force of electric charges in a circuit) cells are connected together in a electrical series with the help och interconnects (bipolar plates) to form a fuel cell stack [7]. Interconnects distribute the electrical current to the cells and separate the atmosphere at the air electrode from the fuel electrode of the next cell. The basic requirements for the interconnect materials are similar to those for electrolytes. Electrolytes need a good ionic conductor and a poor electron conductor, while the interconnect must be a good electron conductor and a poor ionic conductor and can either be made from a ceramic or metallic material [5,7].

2.2.3.1 Ceramic Interconnects:

Ceramic interconnects have long been used with LaCrO3 and widely adapted in high-temperature applications of SOFC [1]. This material exhibits high electric conductivity and can be further improved by doping with Mg, Sr or Ca [1]. Ceramic materials offer high stability on both air and fuel operating sides [7]. The major drawback of using ceramic materials is their cost, manufacturing difficulties and their low mechanical strength [7]. Moreover the electric conductivity of the materials decreases as the pO_2 decreases, becoming lower than those of metals [1,7].

2.2.3.2 Metallic Interconnects:

As the operating temperature of a cell is reduced the use of a metallic interconnect becomes more attractive. Compared to ceramic materials the metallic interconnects have a higher mechanical strength, better electric conductivity and are less expensive to manufacture [1,7]. Metallic interconnects also offer the ability to design flow channels making it possible to control the flow of fuel and air i.e cross, co or counter flow configurations [1]. Interconnects forming a chromia oxide scale have been extensively studied as they exhibit a good oxidation resistance at high operating temperatures [1,7]. However as chromium containing alloys operate for long periods under oxidizing and high temperature conditions the oxide layer on the interconnects surface grows and increases the internal resistance [8]. As the chromium starts to evaporate it's deposited onto the cathode surface leading to a depleted amount of active sites, decreasing the cell performance and long-term stability [1,7,8]. Therefore using

an effective coating on the interconnects surface controls the scale growth and inhibits the evaporation of chromium [8]. High temperature-protective coatings for the alloy interconnects provide low surface resistance and long-term performance [8].

2.2.4 Balance of plant (BOP)

A solid oxide cell (SOC) is not only composed of the SOC stack (anode, cathode, electrolyte and interconnects), the auxiliary components are known as the balance of plant (BOP) [2,7]. The BOP is composed of the cell frame, start-up power source, heat exchangers, steam generators, pipework, pumps, burners, and filters [2,9]. A large part of the BOP is subject to harsh operating conditions and as the shift from ceramic to metallic materials is ongoing, components located upstream of the SOC are often overlooked as a source of volatile chromium [7,9]. BOP unlike interconnects are subject to varying temperatures depending on their functions [9]. Only a few studies have been conducted on the oxidation and chromium evaporation properties of BOP steels, as around 75% of the system manufacturing cost is related to BOP it's important to understand the performance of the used steels [7,9].

2.3 Corrosion of metals

Corrosion is often viewed as wastage of a metal by a corrosive agent, the wider definition is the gradual degradation of a metal by reaction with the environment overtime [7,10]. As metallic materials corrode they convert into their more stable forms (oxides, hydroxides or sulphides) [7]. In essence when a metal corrodes it becomes a charged ion as it loses one or more electrons as seen in equation 4 [10].

$$M \rightarrow M^{a+} + electron \qquad 4$$

At ambient temperature all metals are thermodynamically unstable and form an oxide layer when exposed to oxygen. The growth of the oxide layer is slow and therefore most metals seem to not be affected by oxidation. When temperature is raised the rate of corrosion increases making use of metallic components problematic in high-temperature applications. Important to note is that corrosion of an alloy in high-temperature environments is more complex than corrosion of pure metal [11]. An alloy is a solid solution composed of two or more elements, where at least one of them is a metal. Alloys are typically formed to enhance the properties of the constituent elements, such as strength, hardness, corrosion resistance, or conductivity. Because alloys are composed of different materials they have different affinities

towards oxygen [11]. Therefore diffusion varies through the sample, just like the rate of diffusion varies the oxide formed on or in the sample will vaire [11]. This means that the oxide formed on the surface will not contain the same alloy constituents as the ones formed in the alloy [11]. In the following sections oxidizing behaviors will be described from a thermodynamic and kinetic point of view.

2.4 Thermodynamics

Thermodynamics help predict if a given metal can be oxidized at a given temperature and pressure [7]. Gibbs free energy of a given system helps determine if the formation of an oxide is spontaneous through the use of equation 5 [7,12].

$$\Delta G = \Delta H - T\Delta S \quad (5)$$

Where **Δ**G is the change in gibbs free energy, **Δ**H change in enthalpy, T is the temperature and **Δ**S change in entropy. From equation 5 the possibility of oxide formation can be predicted, if **Δ**G > 0 the reaction isn't spontaneous and if **Δ**G < 0 the reaction is spontaneous (will take place at the given temperature), note that **Δ**G may also be equal to 0 meaning the reaction is at equilibrium [7,12]. One can express gibbs free energy using the reaction quotient Q_p giving equation 6 [12].

$$\Delta G = \Delta G^{\circ} + RTlnQ_p \quad (6)$$

ΔG° is the change in gibbs free energy when all components are under standard conditions, R is the ideal gas constant and T is the given temperature [7,12]. Equation 6 can be simplified further for oxidation of metals but first a general equation for metal oxidation must be defined, see equation 7 [7,12].

$$xM + \frac{y}{2}O_2 \rightarrow M_xO_y \quad (7)$$

Where M represents a given metal, in order to get the equation for gibbs free energy of an oxidizing metal equations 5 & 6 are simply combined giving equation 8 [7,12].

$$\Delta G = \Delta G^{\circ} + RTln\left(\frac{a(M_xO_y)}{a(M)^x * a(O_2)^{\frac{y}{2}}}\right) \quad (8)$$

In equation 8 **a** is the thermodynamic activity of a given species. Approximation for the variable **a** in equation 8 of a pure solid metal and its oxide is set to a=1 [12]. As noted earlier a reaction is at equilibrium when **Δ**G = 0, if this is the case **Δ**G° can be expressed using equation 9 [12].

$$\Delta G^{\circ} = -\ RTln(\frac{1}{a(O_2)^{\frac{y}{2}}}) \qquad 9$$

Further the partial pressure of oxygen can be calculated using equation 10 [12].

$$p_{O_2} = exp(\frac{\Delta G^{\circ}}{RT} * \frac{2}{y}) \qquad 10$$

Form equation 10 one can calculate the thermodynamic stability of a metal/oxide at a given temperature and partial pressure [7,12]. One may also calculate the pO_2 (dissociation pressure) at which the metal and its oxide are at equilibrium [7,12]. In order for oxidation to occur the pO_2 must be higher than the equilibrium partial pressure, meaning that if the pO_2 is below the equilibrium partial pressure the oxide will be reduced to a pure metal [7,12]. One can also without calculations find the pO_2 and ΔG by evaluating the Ellingham diagram in figure 2 [13]. The Ellingham diagram is used to compare the stability of different oxides over a wide temperature and pO_2 range [7,12,13]. If the temperature and pO_2 are known the ΔG of the reaction is easily obtained by drawing a line between the absolute 0 (0K) and the pO_2. Given that the lower the line on the diagram is, the oxide has higher stability and vice versa [7,12]. The oxidation of a metal must also be studied from a kinetic point of view and is done in the coming section.

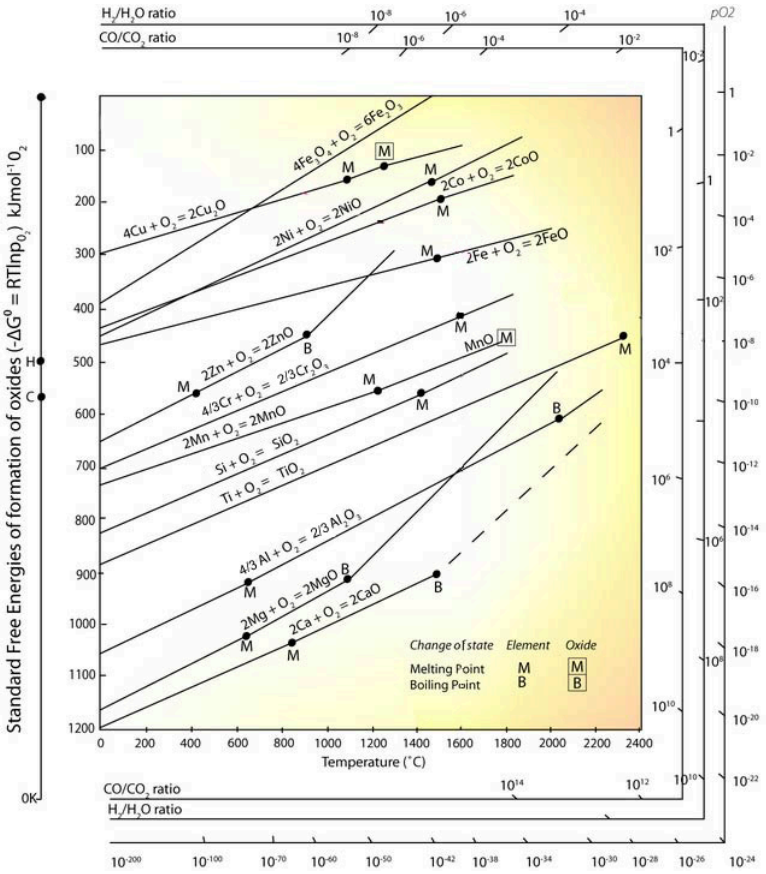

Figure 2: Ellingham diagram shows standard free energy of formation for oxides against temperature[13].

2.5 Kinetics

Observing the Ellingham diagram in figure 2 shows an increase in thermodynamic stability for metals at high temperatures [12]. Since the corrosion of most metals increases at higher temperature this seems contradictory, however from an entropic point of view the increased stability seems intuitive as a solid and gas are combined and form a solid oxide and thus more order is created [12]. The decreased entropy of the system is therefore the driving force of the reaction at high temperature [12]. The observed increase in corrosion rate is because of the increased reaction kinetics [12].

Kinetics help build an understanding of the oxide scale formation and are of use in order to predict the life-span of a component [7,14]. Rate of oxide scale formation is affected by temperature, pO_2, oxidation time and pre-treatments of the metal [7]. When studying the rate of the reaction one can investigate the change in mass, when an oxide is formed the mass increases as the metal reacts with oxygen from the atmosphere [7,12,14]. The measurement of weight gain does however not accurately represent oxidation kinetics in oxide evaporation [7]. Observing the weight difference is not the only method that can be used to observe oxidation kinetics; one can use microscopy, chemical analysis, evaluating the amount of consumed oxygen, etc [7,12,14]. The oxidation growth often fits a linear, parabolic or logarithmic equation (figure 3) [7,12,14]. Oxidation does however follow many different rate equations as the oxidation may occur in two different mechanisms or the rate-determining step changes due to changes in the oxide scale [7,12]. This means that a rate equation may not fit to any of the above mentioned, or they change from for example linear to logarithmic.

Linear rate equation:

Oxidation rates that are limited by interface reactions often proceed at a constant reaction rate and can be described by equation 11 [7,12].

$$x = k_1 t + C \qquad 11$$

Where x is the oxide thickness, k_1 the reaction rate constant, t is the elapsed exposure time and C is the integration constant [7,13,14]. A linear oxidation rate means that the oxidation is independent of the metal consumed, meaning that the oxide scale is not protective[7]. A

linear oxidation rate is often observed when the surface or the phase boundary process is the rate-determining step [7,14].

Parabolic rate equations:

The parabolic rate equation describes an oxidation rate controlled by diffusion through the oxide scale [7,13]. A parabolic rate equation can often be fitted to metals oxidized at high temperatures, described in 1933 by Wagner and derived from fick's law of diffusion [7,13,14]. The model is based on multiple assumptions, the most important being the rate limiting diffusion through the oxide scale and steady state conditions of pO_2 at the metal/oxide and oxide/gas interface [7,13,14]. Calculating the parabolic rate is then done with equation 12.

$$x^2 = k_p t + C \tag{12}$$

Where x is the scale thickness (or the mass gain **Δ**m), k_p is the parabolic rate constant, t is the elapsed time of oxidation and C i the integration constant [7,12,14].

Logarithmic rate equations:

$$\Delta m = k_{log} log(t + t_0) + C \tag{13}$$

In equation 13 **Δ**m represents the samples mass change, k_{log} is the logarithmic rate constant, t is the elapsed exposure time and C is the integration constant [7,14]. As seen in figure 3 the oxidation rate is fast in the initial stages and slows down to negligible changes over time [7,14]. The logarithmic rate equation can often be fitted to metals with thin oxide scales that are in the temperature range of 300-400 ℃ [7,14].

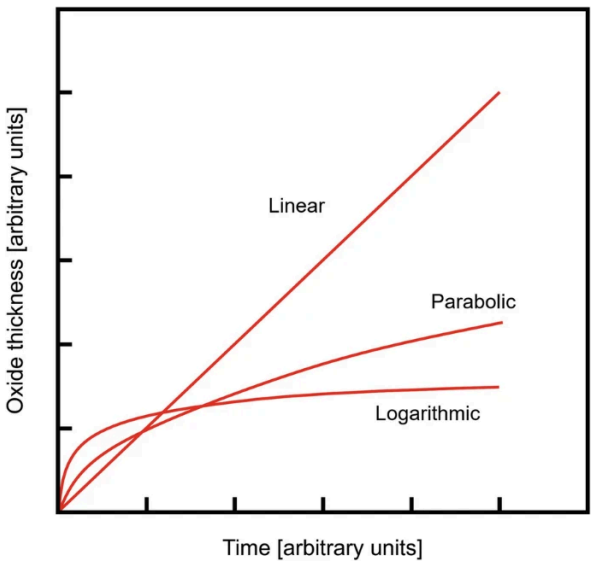

Figure 3: Oxide growth behavior of metal oxides [15]

Important to note is that oxidation behavior outlined in figure 3 might not be what is observed. In figure 4 the theoretical parabolic oxidation behavior is plotted against the real behavior. When the theoretical behavior is compared with the real behavior two different oxidation stages can be identified each with different parabolic constants [15]. The variating behavior of the parabolic rate constant can be attributed to the compositional changes to the base alloy during the process [15]. The other possible phenomenon showcased in figure 4 is the "Real with oxide cracking and spalling" curve, describing the kinetics of cracking and partial spallation of the oxide surface [15]. In figure 4 the "Real with oxide cracking and spalling" curve has sharp drops in weight and can be originated by mechanical stresses associated with thermal cycling [15]. Over time the alloy will no longer be able to provide a sufficient amount of reagents to mend the damaged scale [15].

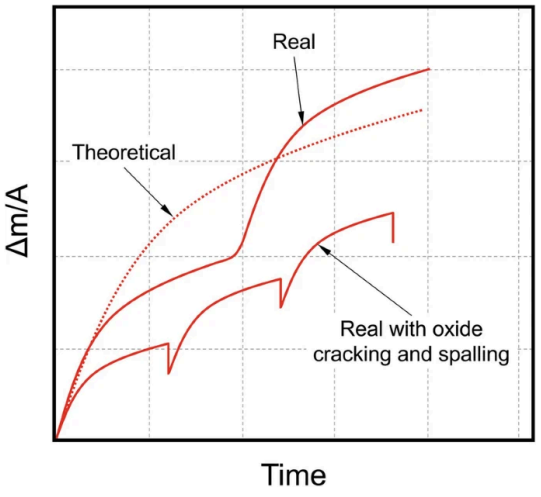

Figure 4: Real Oxide growth behavior of metal oxides [15]

2.6 Scale formation

Oxidation of a metal occurs in three stages as shown in figure 5, adsorption of oxygen gas to the surface followed by oxide nucleation until a continuous film is formed and lastly perpendicular oxide growth of the film [7,12,14]. At stage a) the surrounding oxygen becomes adsorbed to the metal surface [7,14]. As the metal oxide forms the O^{2-} and M^{n+} ions are held together with ionic bonds [7,14]. At the metal-gas interface the metal oxide nucleates and forms a continuous scale along the surface laterally [7,14]. Both steps a) and b) depend on the surface preparation, crystal defects and gas or metal impurities [7,14]. When a continuous oxide film is formed the growth mechanism changes [12]. At this stage the oxygen and the metal have been separated by the oxide film, meaning the continued corrosion is dependent on the oxygen diffusion through the oxide film [12]. Diffusion may either be cation diffusion, oxygen anion diffusion or both [12,14]. In air, diffusion through the oxide scale is often the rate determining step for the oxidation process and as the scale grows thicker the rate of corrosion therefore slows down [12]. The slower rate is referred to as protective oxide behavior [12]. Protective oxides are not always densely packed[12]. One example of such an oxide is Cr_2O_3, with its low density, porosity and ion diffusivity the latter leading to a slow growing oxide scale [14]. Important to note is that with low density and a porous scale the ion diffusivity must be low in order to be protective, a high ion diffusivity would offer less protection against continued corrosion [12]. When Cr_2O_3 is oxidized at high temperature the oxide scale becomes crystalline [12]. Because the scale forms from many different nucleation points (figure 5 b) it will form a polycrystalline film [12]. The polycrystallinity creates many grain boundaries in the scale and allows for easier paths for diffusion in the oxide film (short-circuit diffusion) [12].

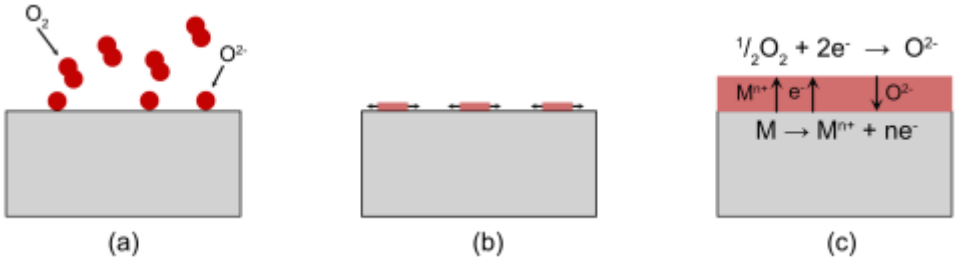

Figure 5: Schematic three step oxide growth process; a) Adsorption, b) oxide nucleation, and c) oxide scale growth [7].

The direction in which an oxide scale grows i.e. inward or outward growing is determined by the ionic diffusion [12]. If diffusion is dominated by oxygen diffusion the oxide is inward growing or if metal ion transport is dominant the oxidation proceeds outwards [12]. Figure 6 shows a simplified model of metal oxide formation at either metal interface in the case of anion mobility or at the oxygen/gas interface in the case of cation mobility [12]. To understand anion and cation transport one must examine the crystal defects in the oxide [12]. Defects are dependent on thermodynamics meaning temperature, pO_2 and energy of formation affect the defect that is to be formed [12]. When a defect is present the diffusion mechanism is affected, determining the scale growth direction [12]. Seen in figure 6 oxides are categorized into n-type and p-type oxides, where n-type oxides carry electrical charges through electrons in the conduction band and p-type oxides carry the charges through electron holes in the valence band [12].

N-type oxide semiconductors are categorized in two groups: metal excess and oxygen deficient. In metal excess oxides, interstitial cations within the lattice are compensated for by an equal charge of electrons in the conduction band, allowing cations to move through the lattice by occupying interstitial sites [12]. Oxygen vacancies in n-type oxides also lead to positive charges, which are balanced by electrons in the conduction band [12]. P-type oxides are characterized by metal deficiency or excess oxygen, resulting in negative charges compensated for by electron holes in the valence band [12]. Excess ions, such as interstitial ions, can diffuse through the oxide by occupying the interstitial sites, while ion vacancies also diffuse within the lattice, leading to conduction of the vacant ion species [12].

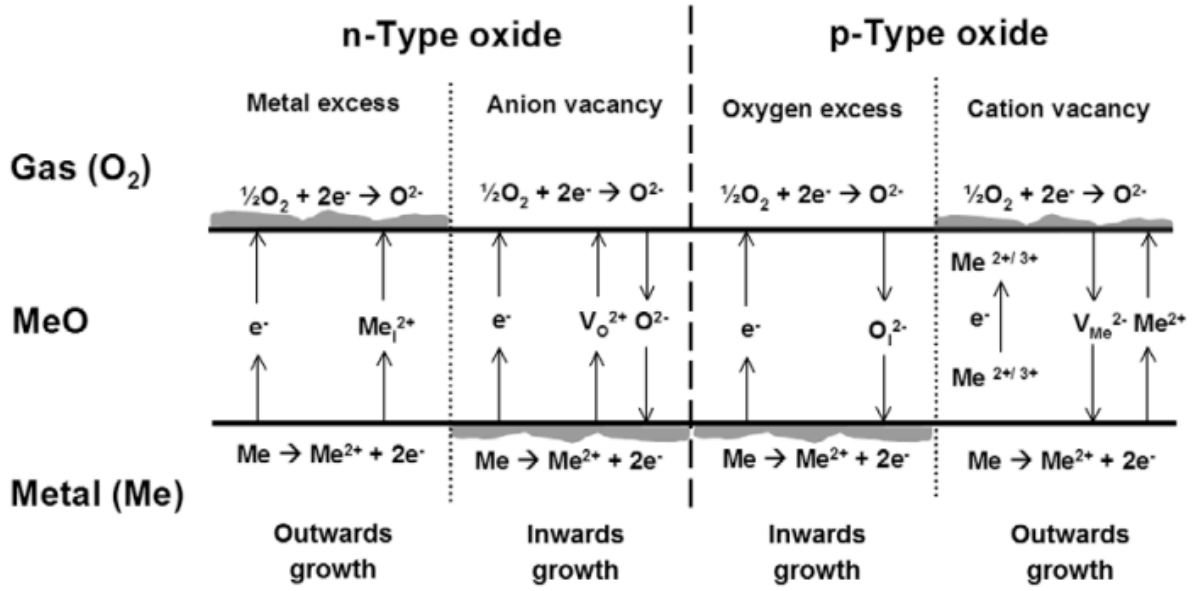

Figure 6: Simplified model of oxide growth direction [12].

2.7 Chromium evaporation

In harsh conditions some oxides react with their surroundings and for volatile metal oxides [7,14]. Some oxides that behave this way are Cr_2O_3, WO_3 and MoO_3, when evaporation takes place the protective oxide scale consumption is accelerated. The evaporation process typically has a high activation energy hence why it is observed at high temperatures [14]. The focus of this chapter will be on chromium evaporation as the mechanism is relevant to the thesis.

Chromium containing alloys form a slow growing and dense protective film (Cr_2O_3) [14]. The film when reacting with oxygen gas at temperatures exceeding 1000 ℃ to form CrO_3 which at the given temperature bears significance on the components lifetime [7,14]. When the Cr_2O_3 film is in the presence of both oxygen gas and water, reactions take place to form $CrO_2(OH)_2$ at much lower temperatures (below 900℃) [7,12,14]. The formation of the volatile species $CrO_2(OH)_2$ occurs by the following reactions (equation 14&15) leading to chromium loss through evaporation [7,12,14].

$$Cr_2O_3(g) + \frac{3}{2}O_2(g) \rightarrow 2CrO_3(g) \qquad 14$$

$$Cr_2O_3(g) + \frac{3}{2}O_2(g) + 2H_2O(g) \rightarrow CrO_2(OH)_2(g) \qquad 15$$

Studies have been conducted and found that the major volatile species formed under atmospheric conditions containing water and oxygen gas is $CrO_2(OH)_2$ [12]. One can note that the partial pressure of the volatile species is directly linked to the partial pressure of water and oxygen gas as can be seen in equation 14&15 [12]. Under normal operating conditions of a SOC the volatile component formed is $CrO_2(OH)_2$ as atmospheric air is always moist to some degree [12]. The partial pressure of the volatile chromium species has a Arrhenius relationship with temperature, meaning that lowering the temperature reduces the problems associated with chromium evaporation [12].

2.7.1 Paralinear oxidation

When a chromia-forming alloy is exposed to high temperatures and a O_2+H_2O environment oxide evaporation takes place at the same time as oxide formation [7]. Seen in figure 6, a metal that follows the paralinear behavior initially gains mass as the oxide scale grows [7]. As the oxide continues to grow thicker the scale growth is at equilibrium with the scale loss through chromium evaporation, when the critical thickness is reached a mass loss is observed as Cr species is continuously evaporated [7]. Parabolic oxidation and linear evaporation is called ’paralinear oxidation’ and is depicted in figure 7 [7].

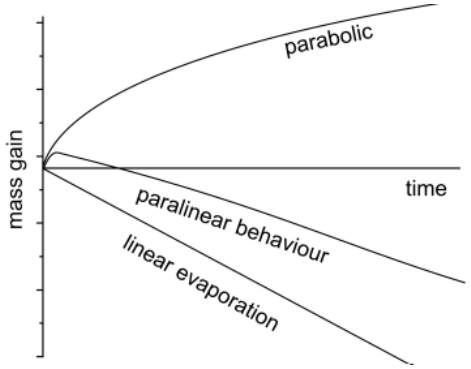

Figure 7: Oxidation behavior over time [7]

2.8 Scanning electron Microscope (SEM)

Scanning electron microscope (SEM) is a non destructive and widely used analytical method [16,17]. With the help of SEM high resolution images and detailed information about a sample's surface morphology is obtained [16,17]. With the use of a focused electron beam, which acceleration voltage can vary from 1keV to 30keV, a significant increase in resolution is observed compared to optical microscopy [16,17]. Using two electromagnetic condenser lenses creates a demagnifide image of an electron source [16]. A third lens focuses the image onto the sample surface [16]. As the scanned beam strikes the sample a variety of signals are generated including secondary electrons, backscattered electrons, and characteristic X-rays [16,17]. The signals are then detected by the appropriate detectors [17]. In figure 8 schematics of a SEM is depicted.

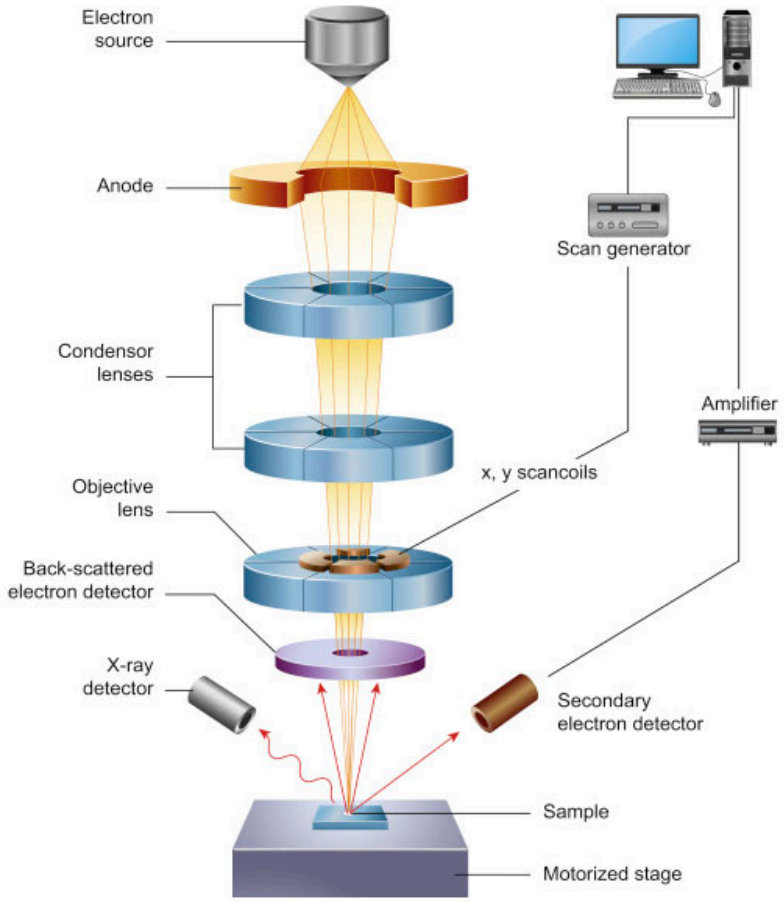

Figure 8: Schematics of a scanning electron microscope [17].

Sample-electron Interaction:

The electron beam only penetrates a few micrometers into the surface when interacting with the atoms in the sample [17]. The extent of the interaction depends on the primary electrons' accelerating voltage and the sample density [17]. As mentioned earlier when the scanned beam strikes the sample a variety of signals are generated including secondary electrons, backscattered electrons, and characteristic X-rays [16,17]. Certain materials may also emit light as the electrons are excited by the beam through a process known as chemiluminescence [17].

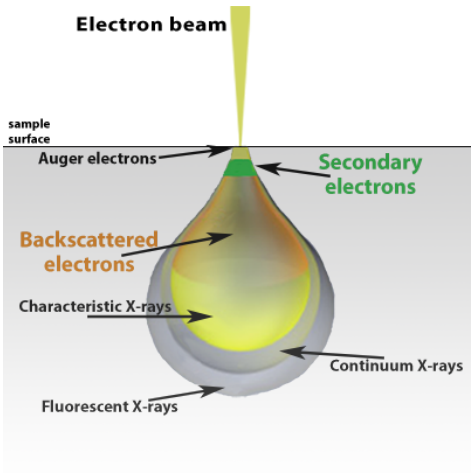

Figure 9: Schematic of electron beam interaction [17].

Secondary electrons are mainly used for topological images because they are generated closer to the material surface [17]. Emissions of secondary electrons occur due to inelastic scattering, or interactions involving energy transfer from a primary beam to an atom in the sample [17]. Secondary electron images give the best lateral resolution as they have a relatively small interaction volume and can be observed in figure 9 above [17].

Backscattered electrons get emitted back above the surface of the sample as can be seen in figure 10 [17]. When the beam approaches the nuclei of an atom the core causes a deflection of the electrons due to charge differences causing the electron to be remitted from the surface [17]. The amount of backscattered electrons is dependent on the atomic number as heavy elements carry more protons hence a higher positive charge in the core. Because of this the image acquired provides information of the surface composition [16,17].

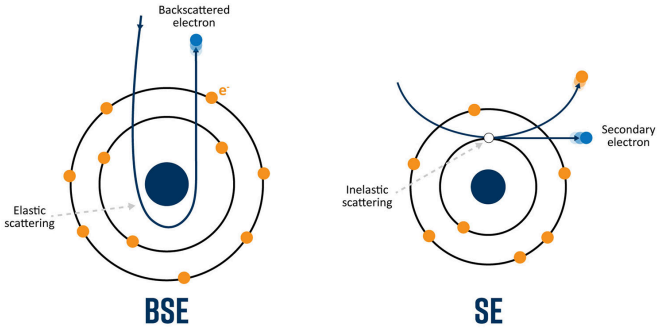

Figure 10: Backscattered electrons vs Secondary electrons generation [17].

X-rays are emitted when atoms are ionized and relax to their ground state again by filling an inner shell electron hole with an electron from a higher orbital [17]. The energy difference between the shells is equivalent to the characteristic x-ray energy and acts as a fingerprint for elements [17]. This means that the emitted x-rays act as a precise identification of the elements present in the sample [17].

3 Method

In this chapter the methodology for reaction kinetics, chromium evaporation and scanning electron microscopy are outlined. It serves as a guide detailing the experimental procedures and the rationale behind the selection of utilized materials. By detailing the methodology, the aim is to provide a clear understanding of the research design and the procedures undertaken to gather and analyze data. Below in table 1 the chemical composition of each compound is shown in wt%.

	C%	P%	N%	S%	Si%	Mn%	Nb%	Cr%	Ti%	Fe	Cu%	Ni%	La%
AISI 441	0,03	0,04	-	0,02	1	1	1	17.5 - 18.5	0.1 - 0.6	Bal	-	-	-
AISI 446	0,2	0,04	-	0,03	1	1,5	0,25	23 - 27	0.1 - 0.6	73	-	-	-
Nirosta (IM1)	0,029	-	0,029	0,09	-	0,35	0,35	20,91	0,129	Bal	0,39	0,18	-
Crofer 22 APU	0,004	-	-	0,01	-	0,38	-	22,92	0,06	Bal	0,01	-	0,09

Table 1: Chemical composition of the used materials in wt%, information from supervisor and [18,19].

The materials chosen for this thesis are AISI 441 (WA), AISI 446 (WE), Nirosta (Industrial melt 1) (WD) and Crofer 22 APU (WC). Crofer 22 APU is currently the market leader and was chosen as a benchmark for the other steels. AISI 441 and 446 are in chemical composition similar to Crofer 22 APU; they are however a cheaper alternative and have therefore been chosen due to the similarity and price point. Nitrosta (IM1) was chosen as it has been shown to perform better than Crofer 22 APU therefore it is tested to see if this is the case.

The received steel sheets were cut into 15x15 mm coupons before the exposure. Cleaning of the samples was performed by ultrasonic agitation first in acetone and then ethanol, the cupones were left to dry on a clean paper cloth before being placed in a clean plastic bag and then weighed (note that the coupons are weighed without the plastic bag!). The samples were not polished or in other ways enhanced/altered before exposure.

Calibration of the furnaces needs to be performed before exposure begins, this is done by measuring the flow using a flowmeter and then inputting the desired temperature of the furnace. With the help of thermometers the hotspot is found (see positioning of thermometer in figure 11). The furnace tubes seen in figure 11 must be moved inward or outward in small increments starting from for example 22cm from the face of the furnace. When the hotspot has been found the temperature can be increased or decreased on the monitor depending on the measured temperature (the temperature should fall in between ±2 ℃ of the exposure temperature).When properly calibrated exposure can begin.

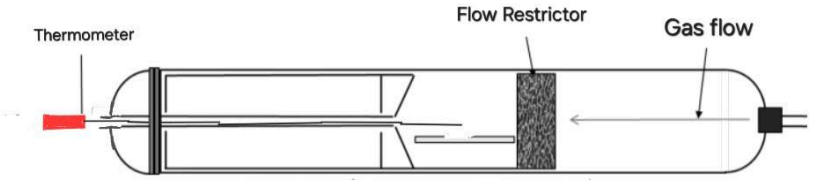

Figure 11: Illustration of where the thermometer should be when calibrating the temperature of the furnace, adapted from [12].

3.1 Reaction kinetics

After the coupons have been cut, cleaned and weighed, three of each coupon are placed on the sample holder in the same fashion as depicted in figure 12. Note that for example coupons WA are not to be placed with WD on two sample holders instead they are placed with WD on one and with WC on another one. This helps identify if the behaviors of the coupons are linked with the samples they are paired with. If sample WA were to be placed with WD on two holders the same behavior would be observed meaning that the influence of the sample WD on the behavior of coupon WA could be mistakenly attributed solely to the WA itself, rather than considering potential interactions between different combinations of samples and coupons. When the coupons have been placed onto the sample holders they are with a flow distributor placed on a silica tube and placed in the furnace at 800˚C after which the flow is turned on, the time is noted and samples are left for the predetermined time (24,168,336,504h).

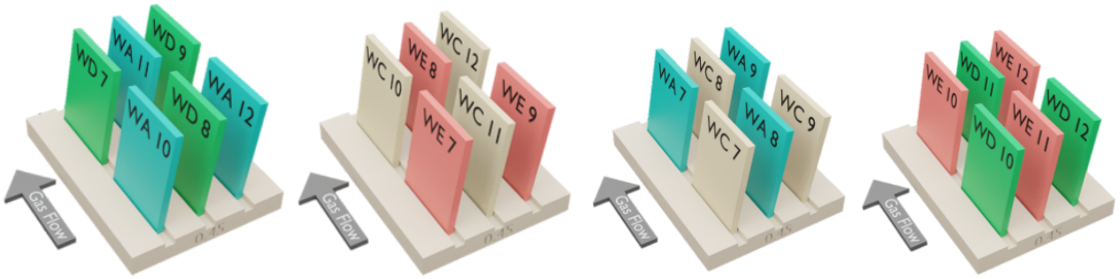

Figure 12: Example of how coupons are to be placed in the sample holders, adapted from supervisor.

The oxidation kinetics were studied using discontinuous mass gain measurements. For this, coupons were removed from the furnace after 24, 168, 336 and 504 hours after they were placed in the furnace. When coupons were removed from the furnace they were removed in increments meaning they were removed in steps out from the furnace and then allowed to cool down to room temperature. The mass of the coupons was measured using an XP6 scale (Mettler Toledo). After recording the mass, the samples were placed back in the furnace and repeated for all the exposure times. The mass gains from the discontinuous mass gain measurements are compared to those recorded after continuous chromium evaporation measurements (see section 3.2 for Cr evaporation method). The mass gains recorded are the sum of mass gained due to oxidation and mass lost due to Cr evaporation. Thus, measured mass gain does not indicate the true extent of oxidation and Cr consumption in the coupon. The mass gain should be compensated by the mass lost due to Cr evaporation to determine the corrected mass gain.

3.2 Chromium evaporation

When preparing for the chromium evaporation experiments the process is similar as for when preparing and executing the reaction kinetics experiment. The furnaces are calibrated, steel sheets are cut, cleaned and weighed in the same way. The preparation differs when the denuder tubes are prepared and 3 coupons of each sheet are used.

Before preparation of denuders begin a solution of sodium hydroxide (NaOH) and methanol (MeOH) is prepared by adding 19,05 grams of NaOH and 80 ml of MeOH to a glass bottle and placing it on a hotplate at 200 ℃ with a stir bar inside and letting sit for 24 hours. When

the solution is done, preparation of the denuders can begin. A Peleus ball is used on the denuder and the solution is pulled up (1 cm from the peleus ball) 2 times, the denuder end that was in the solution is placed on the glass bottle rim before a hair dryer blows hot air through the denuder drying out the solution leaving a semi clear film on the inside. For best result the hairdryer should be place on both openings, when a film is formed CO_2 is allowed to flow through while a heat gun (a Steinel HL1810S heat gun was used at its highest setting) is applied to the tube until the inside changes from semiclear to fully white. The tubes are then placed in a furnace at 120 ℃ (note that these tubes must sit in the furnace for about 24 hours before exposure).

Coupons from the same metal sheet are placed on the sample holder in the center, limiting the number of samples to 3 coupons on each holder. The coupons are placed with a flow distributor on a silica tube and pushed into the furnace at 800 ℃. The denuder tube is inserted through the hole in the silica tube and connected to a wash bottle as seen in figure 14, when the flow is turned on the exposure time is stated.

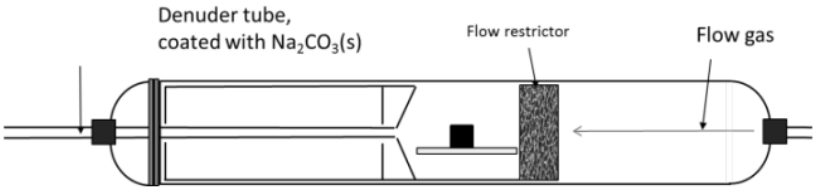

Figure 14: Schematic representation of the chamber when a denuder tube has been attached, adapted from [12].

24 hours after exposure was started the flow was turned off and the denuder changed. Changing the denuder requires 8 volumetric flasks of 25 ml, a marker and deionized water. Each flask is marked with the date, time, furnace (if multiple furnaces are used) and 4 flasks are marked with ‘Den’ (denuder) and 4 with ‘Wash’ or ‘WB’ (wash bottle). The denuder tubes are then placed in the ‘Den’ volumetric flask corresponding to the furnace used and washed with deionized water until the tube is clean. Water from the wash bottle is, with the help of a funnel, transferred to the ‘Wash’ volumetric flask, the walls of the wash bottle are also washed with deionized water and transferred to the volumetric flask until the 25 ml mark is reached. Each volumetric flask is covered with a stopper and the new denuder tubes are placed into the furnaces, the wash bottles are connected to the denuder tubes and the gas flow is turned back on and the time is noted. This is repeated for three weeks and the denuders are

changed about every 48 hours. Exposure was started on a monday and denuders were changed on wednesday and friday until exposure ended. The reaction that is observed in the denuders is described in equation 16.

$$Na_2CO_3(s) + CrO_2(OH)_2(g) \rightarrow Na_2CrO_4(s) + H_2O(g) + CO_2(g) \quad 16$$

Each time a denuder was changed uv/vis-spectroscopy was performed on the samples in the volumetric flasks. Before starting the measurement a blank sample is prepared where milli-Q water is pipetted into a disposable cuvette and the samples from the volumetric flasks are pipetted into a cuvette of their own. Analysis is started at a wavelength of 370 nm and the gathered data is exported to an external drive. The concentration of the sample is calculated by using the Beer-Lambert law seen in equation 17.

$$A = log_{10}\frac{I_0}{I} = \varepsilon_\lambda * c * l \quad 17$$

Where A is the absorbance, I_0 is the intensity of the light for a given wavelength through the pure solvent i.e. milli-Q water and I is the intensity of transmitted light through the solution. ε_λ is the molar absorptivity, l is the path length of the light through the solution, and c is the concentration.

4 Results and Discussion

This chapter presents the results from the oxidation kinetics and Cr evaporation experiments. The results in this section will be accompanied by a comprehensive discussion on some specific topics.

Results from the oxidation kinetics and chromium evaporation were compiled into diagrams listed below. The diagrams for oxidation kinetics show the corrected mass gain (mg/cm^2) over time and the significance of placement for the steel samples. The exact measurements are found in the matlab code in the appendix. Chromium evaporation diagrams are shown where Cr evaporation rate is measured in $mg*cm^{-2}*h^{-1}$ on the Y-axis and time in hours on the X-axis accompanied by a cumulative Cr evaporation diagram beside it. Before discussing the results, the calculations used to obtain the diagrams are presented in section 4.1.

4.1 Calculations

4.1.1 Oxidation kinetics

The diagrams showing the reaction kinetics (Figures 15-16,18-19,21-22 and 24-25) are presented with the cumulative time along the X-axis and the weight change over time ($mg*cm^{-2}$) along the Y-axis. The calculations for this section are seen below starting with determining the surface area of a coupon.

$$A_{surf} = \frac{2*m_{avg}}{\rho*h} \quad (18)$$

In equation 18, m_{avg} represents the average weight of the coupon, ρ is the coupon density and h represents the height (thickness) of the coupon giving the surface area A_{surf}. From equation 18 the final calculation is made in order to get the weight change per unit area seen in equation 19.

$$\sigma = \frac{\Delta m_{avg}*1000}{A_{surf}} \quad (19)$$

In equation 19, σ represents the weight change per unit area (in this case $mg*cm^{-2}$). Δm_{avg} is the average weight change of the coupon when compared to the starting weight and A_{surf} from equation 18 is the surface area of the coupon. From equations 18 & 19 the gathered

information is for each sample, calculations also have to be made for the significance of the sample placement. The calculations begin with calculating the average weight change for the front row/back row samples seen in equation 20

$$\sigma_{avg} = \frac{\sigma_{WA1}+\sigma_{WA2}+\sigma_{WA3}}{x} \quad 20$$

Where σ_{avg} represents the average weight change for the three samples, σ_{WAx} represents the weight change for one sample of the given species and x represents the amount of species. When the average weight change has been obtained the standard deviation can be calculated from a series of equations 21-24 shown below.

$$\bar{x} = \frac{1}{n}\sum_{i=1}^{n} x_i \quad 21$$

$$\sum_{i=1}^{n} (x_i - \bar{x})^2 \quad 22$$

$$s^2 = \frac{1}{n-1}\sum_{i=1}^{n} (x_i - \bar{x})^2 \quad 23$$

$$s = \sqrt{s^2} \quad 24$$

Where $\bar{x}$ is the mean sample weight, n is the number of data points or samples, x_i is each data point and s is standard deviation. Equations 20-24 are carried out for the front and back row of each sample and when plotted against one another giving the significance of placement.

4.1.2 Chromium evaporation

The initial calculations for chromium evaporation calculates the total surface area of the three coupons used and is done by using equation 18 for each coupon and adding them together giving equation 25.

$$A_{tot} = A_{surf\,1} + A_{surf\,2} + A_{surf\,3} \quad 25$$

Where A_{tot} represents the total area of the coupons in the furnace (important to note is that A_{tot} is calculated for only the same coupon species). Calculating the rate of evaporation, the concentration of chromate in ppm needs to be calculated. The concentration of chromate is calculated by applying Beer-Lambert law seen in equation 17. Rearranging the variables gives equation 26.

$$A_{Den/WB} = \varepsilon_{\lambda} * c * l \Rightarrow c = \frac{A_{Den/WB}}{\varepsilon_{\lambda} * l} \quad (26)$$

Where $A_{Den/WB}$ is the absorbance observed from the UV/VIS analysis of the denuder/wash bottle samples, ε_{λ} is the molar absorptivity, l is the path length of the light through the solution, and c is the concentration. Equation 26 is used to calculate the total concentration (ppm) by simply adding the absorbance from the denuder tube to the absorbance from the wash bottle as seen in equation 27. When the total concentration of chromate is calculated the mass is easily calculated with equation 28.

$$c = \frac{A_{Den}}{\varepsilon_{\lambda} * l} + \frac{A_{WB}}{\varepsilon_{\lambda} * l} \quad (27)$$

$$m_{Chromate} = c * V \quad (28)$$

Where $m_{chromate}$ is the mass of chromate from the wash bottle and denuder tube, c is the concentration of chromate and V is the volume of the solution which equals the volume of the volumetric flask in use. When the mass of chromate has been calculated the mass of chromium is calculated per equation 29.

$$m_{Cr} = m_{Chromate} * \frac{52}{116} \quad (29)$$

Where m_{Cr} represents the mass of chromium, $m_{chromate}$ the mass of chromate from the wash bottle and denuder tube and the constant 52/116 represents the molar weight% of chromium in chromate. When the mass of evaporated chromium is obtained the concentration of chromium in mg/cm^2 is calculated using equation 30.

$$c_{Cr} = \frac{m_{Cr}}{A_{tot}} \quad (30)$$

Where c_{Cr} is the concentration of evaporated chromium, m_{Cr} from equation 24 as the mass of evaporated chromium and A_{tot} from equation 25 as the total surface area of all three samples. From equation 30, the rate of evaporation is calculated with equation 31.

$$R_{Cr\ evap} = \frac{c_{Cr}}{t} \quad (31)$$

$R_{Cr\ evap}$ represents the rate of chromium evaporation in the unit mg*cm^{-2}*h^{-1}, c_{Cr} from equation 30 is the concentration of evaporated chromium in mg*cm^{-2} and t is the elapsed time of the measurement. From equation 31 the cumulative chromium is calculated, as shown in equation 32.

$$C_{Cr,i} = R_{Cr\ evap} * t_i + C_{Cr,i-1} \quad (32)$$

$C_{Cr,i}$ represents the cumulative chromium evaporation of the i:th order, meaning the first measurement is the 1:st order. $R_{Cr\ evap}$ from equation 31 is the rate of evaporation, t_i is the

elapsed time for the measurement and $C_{Cr,\,i-1}$ is the cumulative chromium evaporation for the i:th-1 order, meaning that if i=3 then $C_{Cr,\,i-1}=C_{Cr,\,2}$.

After the cumulative chromium evaporation has been calculated one can calculate the corrected mass gain, by calculating σ_{avg} for all samples of the same species as done in equation 20 and the following equation 33 shown below. The standard deviation can also be calculated, seen in equation 21-24.

$$\Delta m_{corrected} = C_{Cr,i} + \sigma_{avg} \quad 33$$

Where $\Delta m_{corrected}$ is the corrected mass gain of the samples $C_{Cr,i}$ is the cumulative chromium evaporation from equation 32 and σ_{avg} is the average mass gain from equation 20.

4.2 Oxidation Kinetics

4.2.1 Corrected mass gain

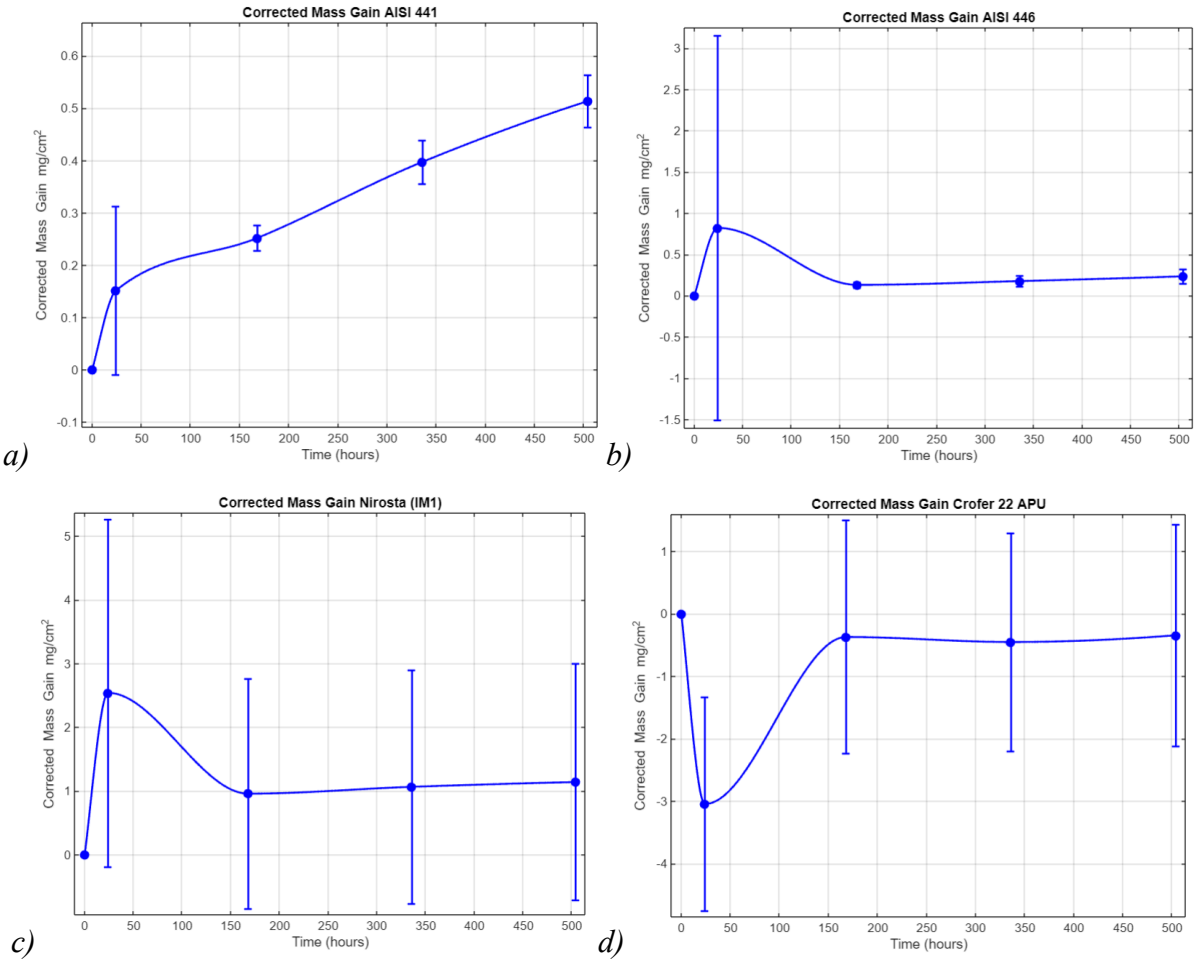

Figure 15: Corrected average mass gain for AISI 441, AISI 446, Nirosta (IM 1) and Crofer 22 APU with standard deviation, exposed to 3% H_2O at a flow of 6000 ml/min and 800 °C for 504h. See Appendix 2 for corrected mass gain data points and code used in matlab.

Figure 15 shows the oxidation kinetics represented by the mass gains of AISI 441, AISI 446, Nirosta (IM 1) and Crofer 22 APU exposed at 800 °C. The mass gain plotted in Figure 15 was measured discontinuously during the exposure. Due to oxide loss through Cr evaporation, the gravimetrically measured mass gain does not indicate the true extent of oxidation. Thus, the mass gain is compensated for with the mass loss due to Cr evaporation, called the ’corrected mass gain’.

At 800 °C, AISI 441, AISI 446, Nirosta (IM 1) and Crofer 22 APU show significant differences in the mass gain, regardless of time. With AISI 441, AISI 446 and Nirosta (IM 1) all showing an increase in mass, while Crofer 22 APU showed a loss in mass followed by a mass gain. The initial loss followed by a mass gain is rather unusual but can be attributed to the samples undergoing thermal stress, leading to spalling of the oxide layer. If spalling occurs, the mass gain from 24 hours to 168 hours in Figure 15d would potentially indicate that a thick oxide scale is formed, leading to potentially higher electrical resistance. Additionally, minor differences in surface roughness or defects could affect how the oxide layer forms and evolves over time. Variations in the microstructure or crystal orientation at the surface could also lead to differences in reactivity with the oxidizing environment. These subtle differences could result in the observed discrepancies in weight change behavior.

AISI 446 and Nirosta (IM 1) seem to follow the same oxidation trend, albeit at different magnitudes. AISI 446 has a lower average mass gain when compared to Nirosta (IM 1), indicating the formation of a thinner oxide scale. Both samples' oxidation rate from the 168th to the 504th hour decreased to a negligible linear rate, suggesting that the scale thickness has likely reached its critical thickness. Further exposure would show a mass loss as Cr species continuously evaporate. The expected outcome would be a ’paralinear oxidation’ and is depicted in figure 7.

When observing the mass gain of AISI 441, a high initial oxidation rate is noted, followed by a linear increase, the mass has increased steadily over the exposure time meaning the oxide scale hasn't reached its critical thickness setting it apart from the other materials.

4.2.2 Significance of placement

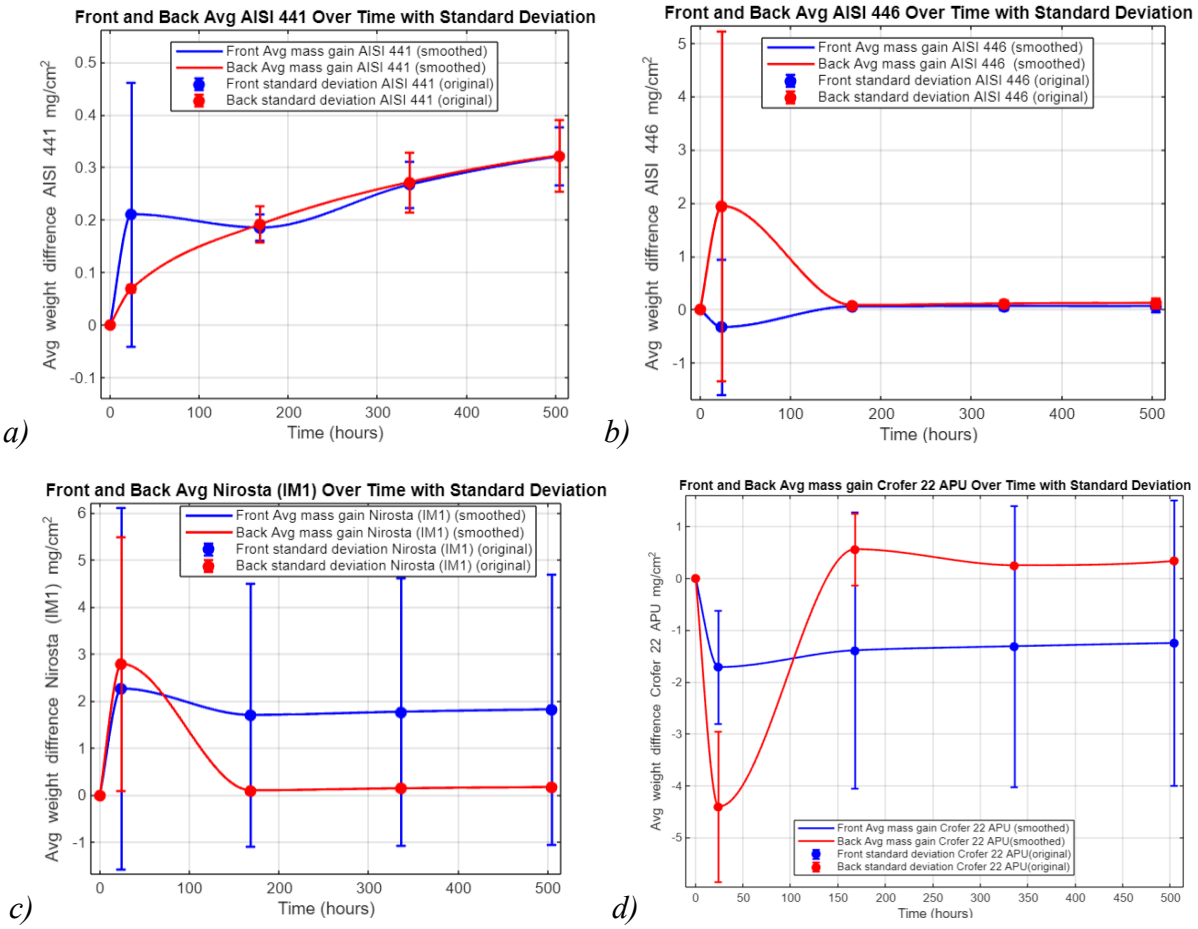

Figure 16: Mass gain for AISI 441, AISI 446, Nirosta (IM 1) and Crofer 22 APU, showing the significance of placement for samples, comparing samples placed on the front and back row, shown with standard deviation. See Appendix 1 for data points and code used in matlab.

This section presents the average mass gain for front row samples compared to the back row samples. The expected outcome is a higher average mass gain for the back row as volatile oxide species are retained in the sample when the atmosphere is saturated with volatile species from the front row.

Figure 16 a) shows the average mass gain with standard deviation for the front and back row of AISI 441. The figure shows a higher average mass gain for the front row samples compared to the back row samples after 24 hours. As the flow reaches the second row, the atmosphere may become saturated with volatile $CrO_2(OH)_2$ from the front row. This leads to less chromium evaporation from the samples in the second row, and thereby, decreasing oxidation rate and mass gain. The samples may also have had slight variations in surface

conditions, such as roughness or pre-existing defects, which can enhance oxidation rates. These surface conditions act as nucleation sites for oxide growth, leading to higher mass gain. This behavior may also be attributed to a wider range of standard deviation than calculated, which requires more experimental work. After the first 24 hours, the back row experiences a similar mass gain to the front row. As the atmosphere becomes slightly less saturated, the evaporation rate increases marginally, resulting in a comparable mass gain in the back row. This occurs because volatile species are both retained in and evaporated from the samples.

Figure 16 b) shows the average mass gain with standard deviation for the front and back row of AISI 446. After 24 hours, a mass loss is observed for the front row, while a mass gain is observed for the back row. This pattern indicates a high initial oxidation rate for the front row. The back row shows higher mass gain. However, the large standard deviation suggests significant variability in mass gain measurements, indicating that results might vary if the experiment is repeated. The nearly identical mass gain measurements after 24 hours imply that oxidation kinetics are similar once the atmosphere isn't saturated when reaching the back row of AISI 446 surface during prolonged exposure. While variation in oxidation kinetics does occur, it does not significantly contribute to the overall mass gain for AISI 446, as evidenced by the difference in mass gains between the front and back rows.

Figure 16 c) shows the average mass gain with standard deviation for the front and back row of Nirosta (IM 1). The back row has a higher mass gain than the front row, with large standard deviations. The initial mass gain for the back row can be attributed to fast oxidation kinetics. This rapid oxidation results in a significant initial increase in mass. The subsequent loss of mass may be due to the evaporation of volatile species within the back row samples as the atmosphere becomes less saturated. In the latter stages of exposure, a higher mass difference is observed in the front row compared to the back row. The notable difference in weight between the front and back rows can be explained by the large standard deviations suggesting variability in the oxidation kinetics in the beginning and latter stages of exposure, which could be due to differences in sample surface conditions, microstructure, or localized defects.

Figure 16 d) shows the average mass gain with standard deviation for the front and back row of Crofer 22 APU. Compared to the other steels, Crofer 22 APU is the only one that initially loses mass; a potential reason for this is mentioned in section 4.2.1. Apart from the initial

mass loss, the front and back row of Crofer 22 APU behave similarly to AISI 441 during the first 24 hours, showing a greater mass loss for the back row compared to the front row, with high standard deviations across the different data points. The front row, however, recorded an overall mass loss, indicating that either the critical scale thickness is thin, leading to mass loss due to chromium evaporation or spallation occurs. In the latter stages of exposure, the difference in mass gain for the back row is substantial. This indicates a decrease in oxidation of volatile species for the back row as the atmosphere is saturated with volatile species, contributing to the higher mass gain. The large standard deviations suggest variability in the oxidation kinetics, which could be due to differences in sample surface conditions, microstructure, or localized defects. These factors highlight the interactions affecting the oxidation behavior and the adherence of volatile species on Crofer 22 APU.

4.3 Chromium evaporation

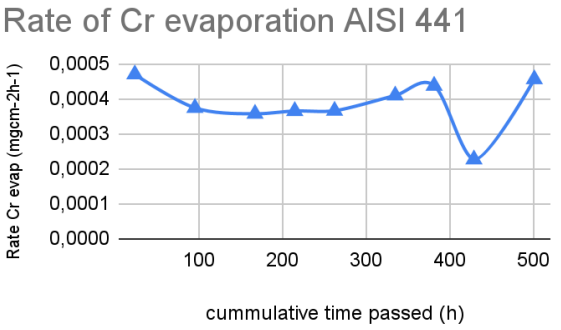

a)

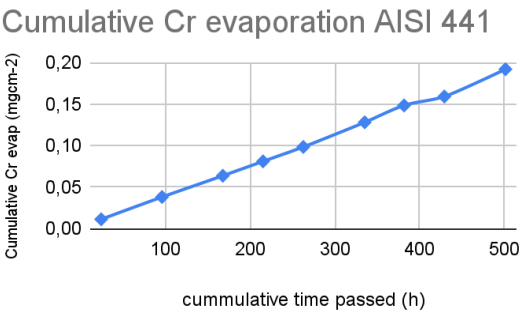

b)

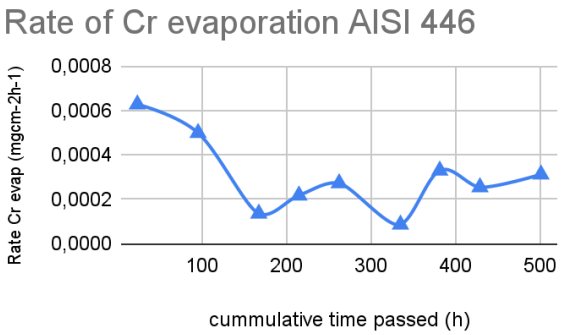

c)

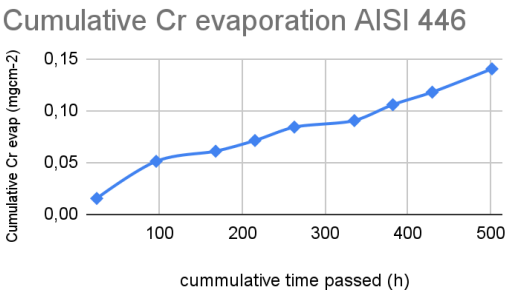

d)

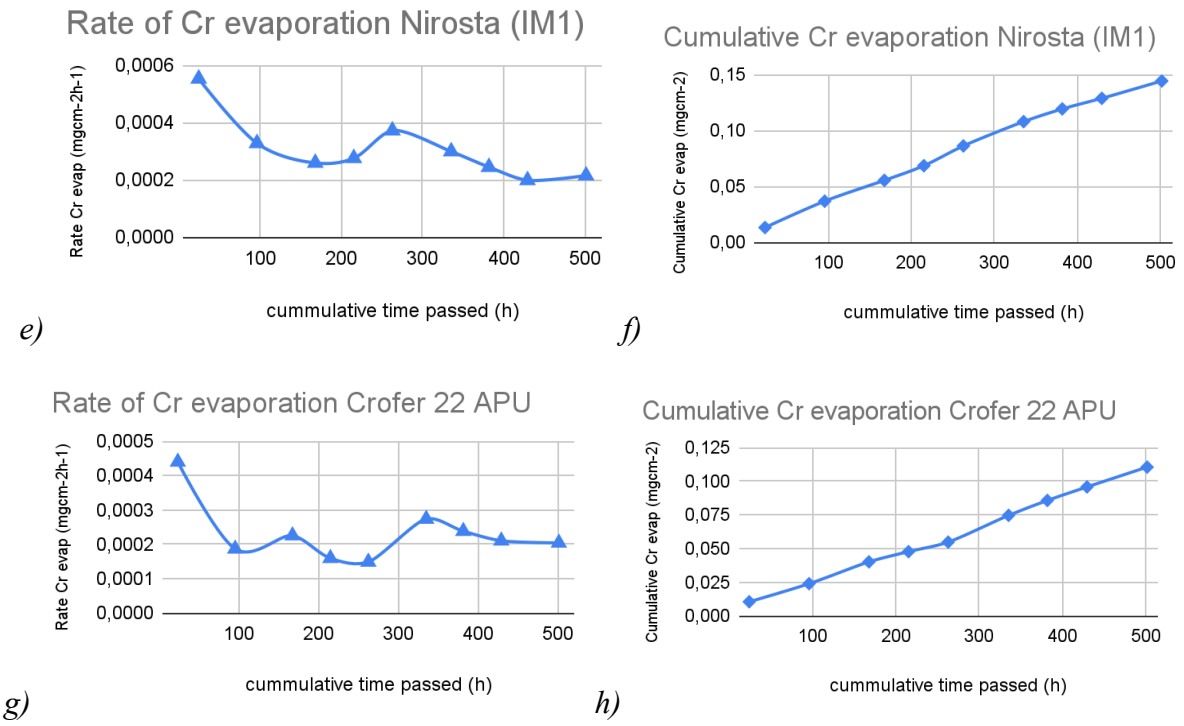

Figure 17: Rate of chromium evaporation and cumulative chromium evaporation for each material over time. In Appendix 3-6 values for the diagrams are found.

Figure 17 presents the rate of evaporation and cumulative evaporation for AISI 441, AISI 446, Nirosta (IM 1) and Crofer 22 APU. Figures 17 a,c,e and g show the rate of evaporation plotted against the exposure time, while figures 17 b, d, f and h show the cumulative chromium evaporation over the exposure time.

At 800 °C AISI 441, AISI 446, Nirosta (IM 1) and Crofer 22 APU all exhibit varying rates of evaporation throughout the exposure time. The expected outcome would be for the rate of evaporation to decrease over time; however, fluctuations were observed instead. Since only one run of each exposure was performed; these fluctuations could be due to inherent variability and are reflected in standard deviation of the samples.

Figure 17a shows the rate of chromium evaporations for AISI 441. A fairly constant and high rate of evaporation is observed in the figure suggesting that the oxide scale formed is rather thin or porous allowing for more evaporation of the volatile chromium species.

Figure 17c shows a high initial rate of evaporation and a drastically lower rate over time for AISI 446. When observing the corrected mass gain of AISI 446 it's not particularly high

indicating a thin and densely packed oxide scale protecting the chromium within the steel from oxidizing at high rates.

Figure 17e illustrates the rate of evaporation for Nirosta (IM 1). A high initial evaporation rate that gradually decreases to a rate similar to that of AISI 446. Unlike AISI 446, which shows a fluctuating rate of evaporation, Nirosta (IM 1) has a consistently decreasing rate. When observing the corrected mass gain of Nirosta (IM 1) it's high, indicating a thicker oxide scale. However, the significance of placement shows that the average weight in the corrected mass gain can be attributed to the front row which has a higher mass gain due to high deviation in measurements. This indicates that Nirosta and AISI 446 are similar to one another with similar oxide scale thickness and therefore protective properties.

Figure 17g shows the evaporation rate of Crofer 22 APU. With the lowest starting rate, Crofer 22 APU outperforms the other steels up to around 350 hours of exposure. After this Nirosta (IM 1) and AISI 446 perform at an equal level to Crofer 22 APU.

According to figures 17 b, d, f and h) the cumulative Cr evaporation is highest for AISI 441 which is to be expected as its rate of evaporation consistently was the highest. This is interesting as AISI 441 is the interconnect that is composed of the least amount of Cr, seen in table 1. This could be due to its scale characteristics meaning if the scale is less dense or has more defects, this could facilitate higher rates of evaporation. Nirosta (IM 1) and AISI 446 both showed similar chromium evaporation rates and subsequently showed very similar cumulative evaporation, as noted earlier they showed similar rates at the latter stages of exposure to that of Crofer 22 APU but had higher cumulative evaporation of chromium attributed to their initial high rate. When observing Figure 15 AISI 446, Nirosta (IM 1) and Crofer 22 APU all have similar mass gain after the exposure but the protectiveness of the scale varies. This indicates that Crofer 22 APU forms a more protective oxide scale quicker while AISI 446 and Nirosta (IM 1) form a similarly protective scale to that of Crofer 22 APU at the later stages of exposure.

5 Conclusion

This thesis investigated candidate materials for interconnects used in solid oxide fuel cells, comparing them against the industry-leading standards. The primary focus was on the air side atmospheres and included investigations into chromium evaporation and oxidation kinetics. The main findings of these studies are summarized below.

AISI 446 and Nirosta (IM 1) exhibited similar oxidation kinetics, albeit at different magnitudes, with Nirosta (IM 1) showing a higher average mass gain compared to AISI 446. In contrast, AISI 441 and Crofer 22 APU show dissimilar oxidation behavior compared to both AISI 446 and Nirosta (IM 1). Figure 15 indicates that AISI 441 hasn't yet reached a critical oxide thickness, suggesting that the oxide scale on this steel will continue to grow if exposure is prolonged. As the scale grows thicker the internal resistance of the interconnect will increase. Crofer 22 APU was the only sample with a mass loss which in section 4.2.1 discussed what could contribute to the behavior. The mass gain is highest for Nirosta (IM 1) followed by AISI 441, AISI 446 and Crofer 22 APU the values are found in appendix 2. As scanning electron microscopy hasn’t been performed it’s not possible to conclude the oxide thickness and therefore predict the interconnect with highest internal resistance. But based on the mass gain, the materials could be arranged as follows: Crofer 22 APU could have the thickest oxide scale, considering the mass gain between 24 and 504 hours is larger than that of the other samples overall. This is followed by Nirosta (IM1), AISI 441 and AISI 446.

The rate of chromium evaporation differed between the investigated steels. AISI 441 had the highest average rate of evaporation followed by Nirosta (IM 1) and AISI 446. Crofer 22 APU had the lowest average rate (the same order is followed for the cumulative chromium evaporation). This indicates that the oxide scale formed by Crofer 22 APU has the best protective properties. Nirosta (IM 1) and AISI 446 both had in the latter stages of exposure a similar rate of evaporation as Crofer 22 APU. This indicates that Nirosta (IM 1) and AISI 446 both formed a protective oxide scale like that of Crofer 22 APU.

The findings suggest that at 800 ℃ a flow of 6000 ml/min and 3% H_2O atmosphere, AISI 441 demonstrates the highest rate of chromium evaporation and Crofer 22 APU the lowest. This indicates the formation of an effective and dense protective oxide scale, making it the

best candidate for interconnect applications in solid oxide fuel cells at the given parameters. The ability of Nirosta (IM 1) and AISI 446 to form protective scales over time also indicates their potential for use in these applications. Considering their price, they emerge as viable alternatives to the more expensive Crofer 22 APU, despite the slight difference in chromium evaporation and scale formation.

6 Future work

Future work that can be conducted on interconnect materials can be focussed on the following:

1. Multiple experimental exposures: Repeating the experiments with multiple runs would help confirm the observed trends and account for any variability in the results. This would give better statistical reliability of the findings.

2. Surface and microstructural analysis: Conducting detailed surface and microstructural analyses using techniques such as scanning electron microscopy (SEM), X-ray diffraction (XRD), and energy-dispersive X-ray spectroscopy (EDS) would provide deeper insights into the oxide scale thickness, composition, and morphology. This information is crucial for understanding the protective properties of the oxide scales.

3. Protective coatings: Exploring the development and application of protective coatings on these interconnect materials could potentially reduce chromium evaporation and enhance their oxidation resistance, thereby improving their overall performance and longevity.

4. Internal resistance: Measuring the internal resistance of the materials discontinuously during the exposure is important for finding the efficiency of the SOFC interconnects, thereby ensuring performance.

Bibliography

1. Nanostructured semiconductor oxides for the next generation of electronics and functional devices [Internet]. Tillgänglig vid: https://www.sciencedirect.com/science/article/pii/B978178242220450007X
2. Shekhawa D, Berr David A, Spive James J. Fuel cells - technologies for fuel processing [Internet]. Elsevier B.V.; Tillgänglig vid: https://app.knovel.com/web/view/khtml/show.v/rcid:kpFCTFP002/cid:kt00BIPZ12/viewerType:khtml/root_slug:fuel-cells-technologies/url_slug:introduction-fuel-processing?&b-q=fuel%20cells&b-toc-cid=kpFCTFP002&b-toc-title=Fuel%20Cells%20-%20Technologies%20for%20Fuel%20Processing&b-toc-url-slug=introduction-fuel-processing&include_synonyms=no&view=collapsed&zoom=1&page=1&q=fuel%20cells
3. Dicks AL, Rand DAJ. Fuel cell systems explained(3rd edition) [Internet]. John Wiley & Sons Ltd; Tillgänglig vid: https://app.knovel.com/kn/resources/kpFCSEE01P/toc?b-q=fuel%20cells&include_synonyms=no&q=fuel%20cells&sort_on=default
4. Administrator. Types of fuel cells [Internet]. 2013 [citerad 25 mars 2024]. Tillgänglig vid:https://www.ceb.cam.ac.uk/research/groups/rg-eme/Edu/fuelcells/types-of-fuel-cells
5. Cassidy M, Connor PA, Irvine JTS, Savani CD. High-temperature solid oxide fuel cells for the 21st century - fundamentals, design and applications [Internet]. Tillgänglig vid: https://app.knovel.com/web/view/khtml/show.v/rcid:kpHTSOFCCA/cid:kt010R6T74/viewerType:khtml/root_slug:high-temperature-solid/url_slug:anodes?&b-q=Solid%20oxide%20fuel%20cells%20SOFC&include_synonyms=no&s_page_no=0&sort_on=default&view=collapsed&zoom=1&page=1&q=Solid%20oxide%20fuel%20cells%20SOFC
6. Haile SM. Materials for fuel cells [Internet]. Tillgänglig vid: https://www.sciencedirect.com/science/article/pii/S1369702103003316#aep-section-id9

7. Reddy M. Metallic materials for solid oxide fuel cells and electrolysers Mitigating high temperature corrosion [Internet]. Chalmers; Tillgänglig vid: https://research.chalmers.se/publication/535305/file/535305_Fulltext.pdf
8. Solid oxide fuel cells - from electrolyte-based to electrolyte-free devices [Internet]. Tillgänglig vid: https://app.knovel.com/web/view/khtml/show.v/rcid:kpSOFCFEB2/cid:kt012EYD45/viewerType:khtml/root_slug:solid-oxide-fuel-cells/url_slug:solid-state-electrolytes?&page=1&b-q=solid%20oxide%20fuel%20cells&view=collapsed&zoom=1&q=solid%20oxide%20fuel%20cells
9. Reddy M, Svensson JE, Froitzheim J. Evaluating candidate materials for balance of plant components in SOFC: Oxidation and Cr evaporation properties [Internet]. Tillgänglig vid: https://www.sciencedirect.com/science/article/pii/S0010938X21004376
10. Schofield MJ. Plant engineer's reference book(Second edition) [Internet]. Tillgänglig vid: https://www.sciencedirect.com/science/article/pii/B9780750644525500882
11. Gao W, Li Z, He Y. Developments in High Temperature Corrosion and Protection of Materials [Internet]. Tillgänglig vid: https://www.sciencedirect.com/science/article/pii/B9781845692193500034
12. Alnegren P. Corrosion of ferritic stainless steel interconnects for solid oxide cells – challenging operating conditions [Internet]. Tillgänglig vid: https://research.chalmers.se/publication/503125/file/503125_Fulltext.pdf
13. Ellingham Diagrams (all content) [Internet]. Tillgänglig vid: https://www.doitpoms.ac.uk/tlplib/ellingham_diagrams/printall.php
14. Claudia Göbel. Corrosion of Ferritic Stainless Steels Used in Solid Oxide Fuel Cells [Internet]. Tillgänglig vid: https://research.chalmers.se/publication/506060/file/506060_Fulltext.pdf
15. Gialanella S, Malandruccolo A. Aerospace alloys [Internet]. Tillgänglig vid: https://link.springer.com/chapter/10.1007/978-3-030-24440-8_8#Sec9
16. Gale WF, Totemeie TC. Smithells Metals Reference Book (8th Edition) [Internet]. Tillgänglig vid: https://app.knovel.com/web/view/khtml/show.v/rcid:kpSMRBE012/cid:kt003OA9NA/viewerType:khtml//root_slug:smithells-metals-reference/url_slug:scanning-electron-microscopy?b-content-type=tsection&b-q=Scanning%20electron%20microscopy&inc

lude_synonyms=no&sort_on=default&view=collapsed&zoom=1&page=7&q=Scanning%20electron%20microscopy

17. Scanning Electron Microscopy [Internet]. Tillgänglig vid: https://www.nanoscience.com/techniques/scanning-electron-microscopy/
18. AISI 441 (1. 4509, x2crtinb18, uns s43940, s43942) [Internet]. Zormetal. [citerad 05 maj 2024]. Tillgänglig vid: https://zormetal.com/en/products/aisi-441-1-4509-x2crtinb18-uns-s43940-s43942/
19. AISI 446 (1. 4762, uns s44600) [Internet]. Zormetal. [citerad 05 maj 2024]. Tillgänglig vid: https://zormetal.com/en/products/aisi-446/

Appendix

Appendix 1. Matlab code for significance of placement

```
%%
% Provided data for Front Avg WA
time_front = [0, 24, 168, 336, 504]; % Time points in hours
data_front = [0, 0.2106765829,0.1853631858,0.2671940523,0.3209912238]; % Data points (Front Avg WA)
std_dev_front = [0, 0.2506605353,0.02491125448,0.04447654243,0.05493782758]; % Standard deviations
% Provided data for Back Avg WA
time_back = [0, 24, 168, 336, 504]; % Time points in hours
data_back = [0, 0.06927059405,0.19141764,0.2720097447,0.3222798155]; % Data points (Back Avg WA)
std_dev_back = [0, 0.006396527708,0.03462737773,0.05671193527,0.06764794269]; % Standard deviations
% Provided data for Front Avg WD
%time_front = [0, 24, 168, 336, 504]; % Time points in hours
%data_front = [0, 2.264425085,1.706299093,1.773436663,1.82439168]; % Data points (Front Avg WD)
%std_dev_front = [0, 3.848430518,2.789545725,2.837259471,2.876730679]; % Standard deviations
% Provided data for Back Avg WD
%time_back = [0, 24, 168, 336, 504]; % Time points in hours
%data_back = [0, 2.790067881,0.1021092312,0.1439931563,0.170525004]; % Data points (Back Avg WD)
%std_dev_back = [0, 2.695579285,0.006853915037,0.0002544581139,0.007625071964]; % Standard
deviations
% Provided data for Front Avg WE
%time_front = [0, 24, 168, 336, 504]; % Time points in hours
%data_front = [0, −0.3295150912,0.05760279827,0.06326951618,0.06397724198]; % Data points (Front Avg
WE)
%std_dev_front = [0, 1.26582117,0.0439221803,0.07510003597,0.1045523943]; % Standard deviations
% Provided data for Back Avg WE
%time_back = [0, 24, 168, 336, 504]; % Time points in hours
%data_back = [0, 1.943412395,0.08327071892,0.1109053325,0.1253194593]; % Data points (Back Avg WE)
%std_dev_back = [0, 3.28713166,0.03416243851,0.06856918513,0.0952082244]; % Standard deviations
% Provided data for Front Avg WC
%time_front = [0, 24, 168, 336, 504]; % Time points in hours
%data_front = [0, −1,711736096,−1.388101952,−1.309566176,−1.24724631]; % Data points (Front Avg WC)
%std_dev_front = [0, 1.096388932,2.669527887,2.712312039,2.753467452]; % Standard deviations
% Provided data for Back Avg WC
%time_back = [0, 24, 168, 336, 504]; % Time points in hours
%data_back = [0, −4.40400768,0.5625471239,0.253342134,0.3355347857]; % Data points (Back Avg WA)
%std_dev_back = [0, 1.453238177,0.6938932446,0.03490498742,0.03763333905]; % Standard deviations
% Interpolation for smoothing
```

```
time_fine = linspace(min(time_front), max(time_front), 500); % Create finer time points
data_front_smooth = interp1(time_front, data_front, time_fine, 'pchip'); % Smooth Front Avg WA data
data_back_smooth = interp1(time_back, data_back, time_fine, 'pchip'); % Smooth Back Avg WA data
% Create a figure
figure;
% Plot the smoothed data with error bars at the original data points
plot(time_fine, data_front_smooth, 'b-', 'LineWidth', 1.5); % Smooth curve for Front Avg WA
hold on;
plot(time_fine, data_back_smooth, 'r-', 'LineWidth', 1.5); % Smooth curve for Back Avg WA
errorbar(time_front, data_front, std_dev_front, 'bo', 'LineWidth', 1.5, 'MarkerSize', 6, 'MarkerFaceColor', 'blue');
% Original points for Front Avg WA with error bars
errorbar(time_back, data_back, std_dev_back, 'ro', 'LineWidth', 1.5, 'MarkerSize', 6, 'MarkerFaceColor', 'red');
% Original points for Back Avg WA with error bars
% Customize the plot
title('Front and Back Avg WA Over Time with Standard Deviation');
xlabel('Time (hours)');
ylabel('Avg weight difference WA');
legend('Front Avg WA (smoothed)', 'Back Avg WA (smoothed)', 'Front Avg WA (original)', 'Back Avg WA
(original)', 'Location', 'best');
grid on;
% Adjust the axis limits for better visualization
xlim([min(time_front)-10, max(time_front)+10]);
ylim([min([data_front-std_dev_front, data_back-std_dev_back])-0.1, max([data_front+std_dev_front,
data_back+std_dev_back])+0.1]);
% Show the plot
hold off;
```

Appendix 2. Matlab code for corrected mass gain

```
% Data sets
data_sets = {
  % Data set WA
  struct('time', [0, 24, 168, 336, 504], ...
       'data', [0, 0.1512385374, 0.252101698, 0.3976569164, 0.5136398268], ...
       'std_dev', [0, 0.1611090312, 0.02481342513, 0.04168052942, 0.05031783779], ...
       'title', 'Corrected Mass Gain AISI 441'),
  % Data set WE
  struct('time', [0, 24, 168, 336, 504], ...
       'data', [0, 0.8220033251, 0.1310607561, 0.1772538191, 0.2347539086], ...
       'std_dev', [0, 2.329677181, 0.03459461297, 0.06336041561, 0.08721230776], ...
       'title', 'Corrected Mass Gain AISI 446'),
  % Data set WC
  struct('time', [0, 24, 168, 336, 504], ...
       'data', [0, -3.047315861, -0.3726007384, -0.4534245657, -0.3453346722], ...
       'std_dev', [0, 1.707846071, 1.867408261, 1.75022539, 1.775940716], ...
       'title', 'Corrected Mass Gain Crofer 22 APU'),
  % Data set WD
  struct('time', [0, 24, 168, 336, 504], ...
       'data', [0, 2.540519073, 0.9596459802, 1.06664769, 1.141739468], ...
       'std_dev', [0, 2.725422927, 1.799229573, 1.82951323, 1.855361041], ...
       'title', 'Corrected Mass Gain Nirosta (IM1)')
};
% Loop through each data set
for i = 1:length(data_sets)
  % Create a new figure for each data set
  figure;
  % Extract data for current figure
  time = data_sets{i}.time;
  data = data_sets{i}.data;
  std_dev = data_sets{i}.std_dev;
  title_str = data_sets{i}.title;

  % Interpolation for smoothing
  time_fine = linspace(min(time), max(time), 500); % Create finer time points
  data_smooth = interp1(time, data, time_fine, 'pchip'); % Smooth Corrected Mass Gain data

  % Plot the smoothed data with error bars at the original data points
  plot(time_fine, data_smooth, 'b-', 'LineWidth', 1.5); % Smooth curve for Corrected Mass Gain
  hold on;
  errorbar(time, data, std_dev, 'bo', 'LineWidth', 1.5, 'MarkerSize', 6, 'MarkerFaceColor', 'blue'); % Original
points for Corrected Mass Gain with error bars

  % Customize the plot
  title(title_str);
  xlabel('Time (hours)');
  ylabel('Corrected Mass Gain mg/cm^2');
  grid on;

  % Adjust the axis limits for better visualization
```

```
    xlim([min(time)-10, max(time)+10]);
    ylim([min(data-std_dev)-0.1, max(data+std_dev)+0.1]);

    hold off;
end
```

Appendix 3. Chromium evaporation data for AISI 441

cumulative time passed (h)	Rate of Cr evaporation ($mgcm^{-2}h^{-1}$)	Cumulative Cr evaporation ($mgcm^{-2}$)
24	0,0004693728722	0,01126494893
95,83333333	0,0003734966113	0,03809445551
167,6666667	0,0003566147975	0,06371128513
215,1666667	0,0003645480906	0,08102731943
262,75	0,0003652428709	0,09840679271
335,25	0,0004089410381	0,128055018
381,75	0,0004368198533	0,1483671412
429,3333333	0,0002262163145	0,1591312674
501,5	0,0004555155615	0,1920043071

Appendix 4. Chromium evaporation data for AISI 446

cumulative time passed (h)	Rate of Cr evaporation (mgcm-2h-1)	Cumulative Cr evaporation (mgcm-2)
24	0,0006272780576	0,01505467338
95,83333333	0,0004987530972	0,05088177086
167,6666667	0,0001356226448	0,06062399751
215,1666667	0,0002173405155	0,070947672
262,75	0,0002723549615	0,08390722892
335,25	0,00008633332212	0,09016639477
381,75	0,0003294384767	0,1054852839
429,3333333	0,0002545508627	0,1175976625
501,5	0,0003118876974	0,140105558

Appendix 5. Chromium evaporation data for Nirosta (IM 1)

cumulative time passed (h)	Rate of Cr evaporation (mgcm-2h-1)	Cumulative Cr evaporation (mgcm-2)
24	0,0005530245685	0,01327258964
95,83333333	0,0003278997197	0,03682671951
167,6666667	0,0002591429032	0,05544181806
215,1666667	0,0002757376219	0,0685393551
262,75	0,0003721745493	0,08624866073
335,25	0,0002990913098	0,1079327807
381,75	0,0002447019151	0,1193114197
429,3333333	0,0001985432523	0,1287587695
501,5	0,0002150903844	0,1442811256

Appendix 6. Chromium evaporation data for Crofer 22 APU

cumulative time passed (h)	Rate of Cr evaporation (mgcm-2h-1)	Cumulative Cr evaporation (mgcm-2)
24	0,0004398344729	0,01055602735
95,83333333	0,0001868552365	0,02397846184
167,6666667	0,0002254971771	0,04017667573
215,1666667	0,0001595776055	0,04775661199
262,75	0,0001488576996	0,05483975753
335,25	0,0002737613508	0,07468745546
381,75	0,0002383335547	0,08576996576
429,3333333	0,0002104665141	0,09578466405
501,5	0,0002041998986	0,1105210901